
# Prise en compte des effets d'installation dans une soufflerie anéchoïque pour la caractérisation de sources aéroacoustiques

A. Pereira[a], A. Finez[b], C. Picard[b], Q. Leclere[a], J. Antoni[a], P. Souchotte[c], M. Roger[c] et I. Aparicio[a]

[a]Laboratoire Vibrations Acoustique, INSA de Lyon Bâtiment St. Exupéry 25 bis av. Jean Capelle, 69621 Villeurbanne, France

[b]MicrodB, 28, chemin du petit bois, 69130 Écully, France

[c]École Centrale de Lyon - LMFA, 36. Av. Guy de Colongue, 69131 Écully, France

antonio.pereira@insa-lyon.fr

Dans le cadre du projet SEMAFOR, des mesures acoustiques à l'aide d'une antenne de microphones ont été réalisées dans une soufflerie anéchoïque à l'Ecole Centrale de Lyon (ECL). Le protocole expérimental est constitué d'un profil NACA 0012 fixé entre deux plaques de maintien et d'une antenne de microphones positionnée parallèlement au profil, à une distance d'environ une envergure, soit trois fois la corde. Un écoulement d'air est généré par une petite soufflerie permettant de contrôler sa vitesse. Plusieurs conditions d'écoulement correspondant à différents mécanismes aéroacoustiques ont été testées. Cette étape préliminaire a pour but la caractérisation de sources à l'aide des méthodes d'imagerie acoustique, afin de valider des modèles de source potentiels. L'objectif de cette contribution est d'étudier l'effet du confinement dû aux plaques de maintien sur les méthodes d'imagerie acoustique. Pour cela, la propagation acoustique en prenant en compte la géométrie des plaques, est calculée numériquement par la méthode des éléments de frontière (BEM) ainsi qu'analytiquement par la méthode des sources images. Les modèles de propagation développés permettent d'évaluer l'influence des réflexions et de la diffraction des ondes acoustiques au niveau des bords des plaques. Dans un deuxième temps, ces modèles de propagation sont implémentés dans les méthodes d'imagerie acoustique afin d'estimer le gain en performance par rapport aux modèles simplifiés.

# 1 Introduction

Over the last decades, several methods dedicated to acoustic imaging have been developed and applied in aeroacoustics [1, 2, 3]. The basic principle of acoustic imaging is to use the information (pressure or particle velocity) delivered by an array of sensors in order to reconstruct acoustical quantities (e.g. normal velocity, pressure, acoustic power) on a surface representing a physical source. The reconstructed source quantities may be used not only to localize the main radiating regions but also, at some extent, to quantify the identified sources. A simplifying hypothesis, which is common to most acoustic imaging methods, is the assumption that the wave propagation from sources to microphones takes place in free-field conditions. Although this assumption leads to a considerable simplification of algorithms, it may lead to improper source localization and quantification. Within the framework of the project SEMAFOR, preliminary aeroacoustic measurements were conducted in an open-jet anechoic wind tunnel at the Ecole Centrale de Lyon (ECL). The aim of such experiments being the use of acoustic imaging techniques to help in understanding different aeroacoustic mechanisms and eventually provide empirical models which characterize them. The experimental set-up is shown in in Figs. 1 and 2. A rectangular nozzle of width 15cm is used to direct the flow and two side-plates extending the nozzle lips help to fix obstacles in the flow region. An acoustic array consisting of 54 microphones is placed parallel to the flow direction at a distance of 35cm from the potential core of the rectangular jet (see Fig. 2).

Figure 1: Side view of the experimental set-up showing a NACA 0012 airfoil placed in the open-jet anechoic wind tunnel of ECL.

Previous studies on a similar experimental set-up with a larger rectangular nozzle have shown that diffraction effects at the nozzle lips significantly alter the directivity of the sound emitted by an airfoil [4, 5]. The aim of this contribution is to evaluate the confinement effect introduced by the two side-plates on the acoustic imaging results. For that purpose, a numerical approach using the Boundary Element Method (BEM) and an analytical approach based on the concept of image sources (ISM) are used to model the effect of the two plates. The BEM model is used for the low to mid-frequency range (500 Hz - 3 kHz) and the image source method for higher frequencies. This paper is organized as follows. In Section 2 we briefly explain the boundary element method and the image source method used to model the geometry of the problem. Section 3 is dedicated to a validation of both models with a controlled experiment using an artificial source. Finally, in Section 4 we present acoustic imaging results using the propagation models for aeroacoustic sources.

Figure 2: Front view of the experimental set-up.

# 2 Modeling of the problem geometry

## 2.1 Boundary Element Method

In this section we use the boundary element method (BEM) to compute the propagation of acoustic sources located in between the two side plates. The method employed here is based on the Kirchhoff-Helmholtz integral equation with rigid surfaces. The acoustic pressure at a position $\mathbf{x}$ in space is written as:

$$\sigma(\mathbf{x})p(\mathbf{x}) = p^i(\mathbf{x}) - \int_\Gamma p(\mathbf{y})\frac{\partial G(\mathbf{x}|\mathbf{y})}{\partial n}d\Gamma(\mathbf{y}), \qquad (1)$$

where $\sigma(\mathbf{x})$ is a coefficient related to the solid angle, $p^i(\mathbf{x})$ is the incident pressure and the second term on the right hand side expresses the effect of the rigid surfaces. The collocation method allows one to discretize the surface integral by using a linear interpolation of the acoustic pressure based on the pressure at the surface nodes ($\mathbf{y}_n$). The problem then writes:

$$\sigma(\mathbf{x})p(\mathbf{x}) = p^i(\mathbf{x}) - \sum_n p(\mathbf{y}_n)a_n(\mathbf{x}), \tag{2}$$

with $\mathbf{y}_n$ the position of the $n$-th node. In a first step we compute the transfer matrix between the incident pressure and the resulting pressure at the nodes on the boundary

$$\sigma(\mathbf{y}_m)p(\mathbf{y}_m) = p^i(\mathbf{y}_m) - \sum_n p(\mathbf{y}_n)a_{mn}, \tag{3}$$

which can be written in matrix form as:

$$\mathbf{\Sigma p}_y = \mathbf{p}_y^i - \mathbf{A p}_y. \tag{4}$$

The above equation can be inverted in order to obtain the transfer matrix $\mathbf{B}$:

$$\mathbf{p}_y = (\mathbf{\Sigma} + \mathbf{A})^{-1}\,\mathbf{p}_y^i = \mathbf{B p}_y^i. \tag{5}$$

The estimation of $\mathbf{B}$ based on the inversion of the above matrix may be ill-conditioned at the eigen frequencies of the volume interior to the boundaries. To avoid this limitation, few additional nodes are randomly placed in the interior volume and forced to a zero pressure. An extended system is thus written:

$$\left\{ \begin{array}{c} \mathbf{\Sigma p}_y \\ \mathbf{p}_v \end{array} \right\} = \left\{ \begin{array}{c} \mathbf{p}_y^i \\ \mathbf{p}_v^i \end{array} \right\} - \left[ \begin{array}{c} \mathbf{A} \\ \mathbf{A}_v \end{array} \right] \mathbf{p}_y, \tag{6}$$

where the subindex $v$ refers to the interior volume. Rearranging Eq. (6) leads to the following relation:

$$\mathbf{p}_y = \left( \left[ \begin{array}{c} \mathbf{\Sigma} + \mathbf{A} \\ \mathbf{A}_v \end{array} \right] \right)^{-1} \left\{ \begin{array}{c} \mathbf{p}_y^i \\ \mathbf{p}_v^i \end{array} \right\} = [\mathbf{B}] \left\{ \begin{array}{c} \mathbf{p}_y^i \\ \mathbf{p}_v^i \end{array} \right\}. \tag{7}$$

Finally, the acoustic pressure at any point in space may be written as a function of the incident pressure:

$$p(\mathbf{x}) = p^i(\mathbf{x}) - \mathbf{a}_x^T \mathbf{p}_y = p^i(\mathbf{x}) - \mathbf{a}_x^T \mathbf{B p}_y^i. \tag{8}$$

The BEM model of the side plates along with the position of microphones are shown in Fig. 3. A spatial resolution of 2 cm is used to discretize the boundaries, which respects a condition of 6 elements per wavelength up to approximately 3 kHz. We point out that some simplifications are made at this stage: the geometry of the airfoil itself and the nozzle lips are not taken into account in the model.

The geometry of the problem has also been modeled with the Finite Element Method (FEM) for validation purposes. The FEM model is implemented in Actran. The frequency response at a microphone's position due to a monopole source located in between the two plates is computed by both methods. Fig. 4 shows the acoustic pressure at a microphone located on the lower part of the array. We can see that results obtained by BEM and FEM are in relatively good agreement up to 2 kHz. Similar results were obtained for the ensemble of microphones on the array.

Although the numerical approaches provide an accurate model of the problem geometry, they become computationally expensive for higher frequencies, because the number of elements needed to respect a discretization rule is excessively large. A different model, based on the concept of image sources is then used for higher frequencies.

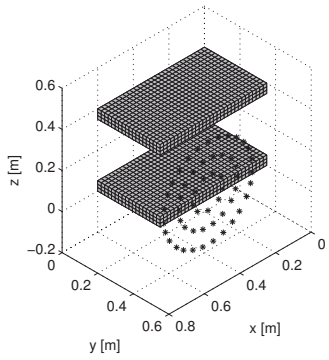


Figure 3: Discretization of the side-plates geometry used in the BEM model.

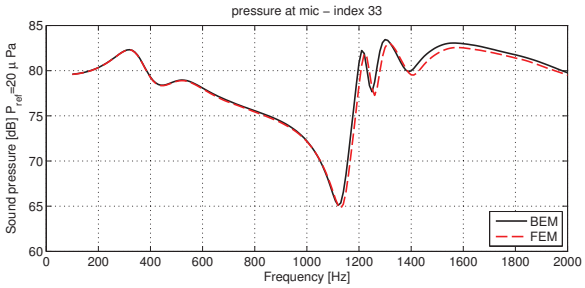


Figure 4: Acoustic pressure at a microphone position computed by BEM and FEM.

## 2.2 Image Source Method

The second approach used to model the effect of side plates is based on the concept of image sources. The basic idea is to replace the boundaries of the plates by a finite number of image sources. The acoustic pressure at a single microphone $p(\mathbf{r}_i)$ due to a unit point source located at $\mathbf{r}_s$ is written as a sum of the direct field plus the contribution of image sources such as

$$p(\mathbf{r}_i) = \frac{\mathrm{j}\omega\rho}{4\pi} \left[ \frac{e^{-\mathrm{j}k\|\mathbf{r}_i - \mathbf{r}_s\|}}{\|\mathbf{r}_i - \mathbf{r}_s\|} + \sum_{n=1}^{N} \frac{e^{-\mathrm{j}k\|\mathbf{r}_i - \mathbf{r}_n\|}}{\|\mathbf{r}_i - \mathbf{r}_n\|} \beta^{O(n)} \right], \tag{9}$$

where $\beta$ is a reflection coefficient and $O(n)$ is the order of the $n$-th image source. It is assumed hereafter that there is no dissipation at the surface of the plates and that reflections are angle independent. Furthermore, only first order image sources are used and their contribution is truncated to a defined ensemble of microphones, to account for the finite length of the plates. The above is done to consider the fact that lower microphones (resp. upper microphones) "do not see" the lower image (resp. upper image). We finally remark that diffraction and scattering effects are not taken into account in this case.

# 3 Validation using an artificial source

In order to check the validity of the previous approaches, a validation measurement with an artificial source has been carried out. The physical source consists of a tube of small diameter connected to a driver unit. A reference pressure microphone is placed near the tube opening, as shown in Fig. 5 and is used to get a rough estimate of the volume velocity of the source. The source is placed near the airfoil trailing

edge, with the opening facing the array at a midspan position. These validation measurements are carried out without the airflow.

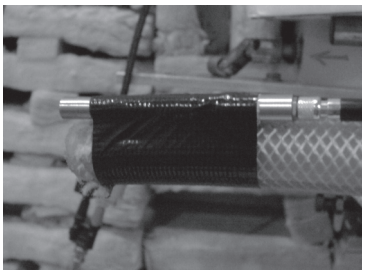

Figure 5: Small diameter tube used as an artificial source. The figure also shows the reference microphone near the tube opening.

The propagation models developed in previous sections and the estimate of the source's volume velocity are used to simulate the acoustic pressure at the position of microphones. The experimentally simulated acoustic pressure is then compared to the measured one, as shown in Fig. 6. One can notice several interference dips on the measured PSD due to a complex acoustic propagation in between the side plates. We can also see that the simplified image source model is not able to predict the first interference dip around 1200 Hz, which is certainly due to a diffraction effect. On the other hand, the image source method estimate relatively well the interferences above 2000 Hz. The acoustic pressure computed by BEM is in better agreement with the measured pressure at lower frequencies.

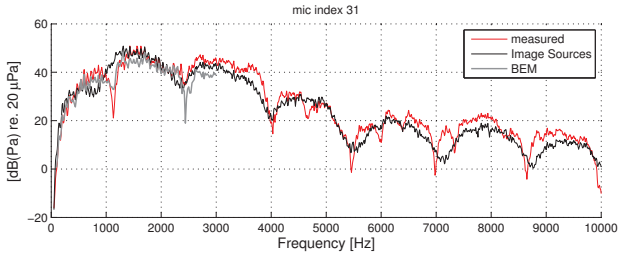


Figure 6: PSD of the acoustic pressure at a microphone position for: (a) measured; (b) computed by the image sources model and (c) computed by BEM

## 3.1 Acoustic imaging results

In this section we investigate the use of propagation models taking into account the side plates for acoustic imaging purposes. A distribution of equivalent sources is placed on a plane parallel to the array and containing the tube opening. A model relating each equivalent source to the microphones is established and we have in matrix form:

$$\mathbf{p} = \mathbf{G}\mathbf{q} + \mathbf{n}, \tag{10}$$

where $\mathbf{p} \in \mathbb{C}^M$ is a vector of complex measured acoustic pressure, $\mathbf{q} \in \mathbb{C}^N$ the amplitude of equivalent sources, $\mathbf{n} \in \mathbb{C}^M$ accounts for measurement noise and $\mathbf{G} \in \mathbb{C}^{M\times N}$ is a propagation matrix. Since the number of equivalent sources used to discretize the source region is larger than the number of microphones (i.e. $N \gg M$), the system is underdetermined and thus have an infinite number of solutions. Moreover, the inversion of matrix $\mathbf{G}$ is well-known to be ill-posed, in the sense that it is highly sensitive to measurement noise in $\mathbf{p}$. Additional *a priori* information on the solution is thus required to solve the above problem. One alternative is to impose a constraint on the energy of the solution, which leads to the following well-known Tikhonov solution:

$$\hat{\mathbf{q}} = \mathbf{G}^H(\mathbf{G}\mathbf{G}^H + \eta^2\mathbf{I})^{-1}\mathbf{p}, \tag{11}$$

where the difficulty remains on the selection of a reasonable regularization parameter $\eta^2$ [6]. This is done here by using a criterion derived from a Bayesian approach and we refer the reader to refs. [7, 8] for more details. A source plane of dimensions 1m×1m is discretized with a regular spacing of 2cm. An estimate of the source field is obtained via Eq. 11 considering different acoustic propagation models: (a) free-field Green's function; (b) propagation computed by BEM and (c) propagation computed by the image source method. The reconstructed source field considering a free-field propagation is shown in Fig. 7 for a frequency band from 1000Hz to 1200Hz. We notice that along with the original source, additional sources are reconstructed at the exterior of the plates. Similar results were obtained for frequencies ranging from 1000Hz up to 2000Hz and are not shown here.

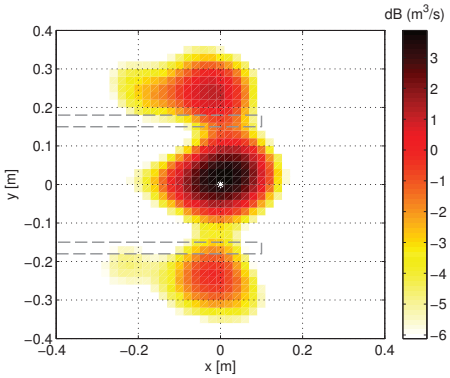


Figure 7: Volume velocity map integrated over the 1200-1400 Hz frequency band for a free-field Green's function. The position of the artificial source is marked by a white dot and the dynamic range is 10 dB.

Fig. 8 shows the results for the propagation matrix computed by BEM. We notice that the effect of the secondary sources is attenuated in this case, illustrating the benefit of using a more complex propagation model. One may ask if the same result could be obtained by simply truncating the source plane to the region between the plates. The above was tested but the results were not satisfactory; all the energy of the reconstructed field was essentially concentrated on the boundaries of the truncated source plane, at the vicinity of the plates. Conversely, the truncation of the source region may be advantageous for approaches such as beamforming, which solves the problem independently for each grid point on the source plane. The limitation of beamforming as compared to the present approach being its inferior spatial resolution at low frequencies and non-quantitative results.

The reconstructed source field at a higher frequency band is shown in Fig. 9 in the case of a free-field propagation. We notice again the identification of additional sources at

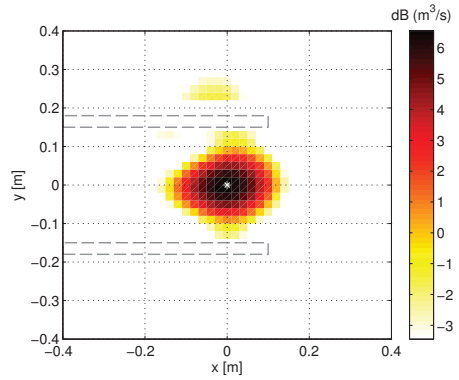


Figure 8: Volume velocity map integrated over the 1200-1400 Hz frequency band for a propagation computed by BEM.

the proximity of the plates. At this frequency range, the image source model was used to model the wave reflections and the reconstructed source is shown in Fig. 10. We still notice some residual contribution at the position of the image sources, although with an increased dynamic range (12 dB) as compared to the free-field case (5 dB).

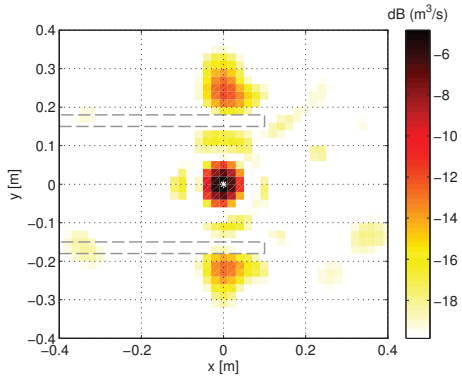


Figure 9: Volume velocity map integrated over the 4000-4500 Hz frequency band for a free-field Green's function. The dynamic range is 15 dB.

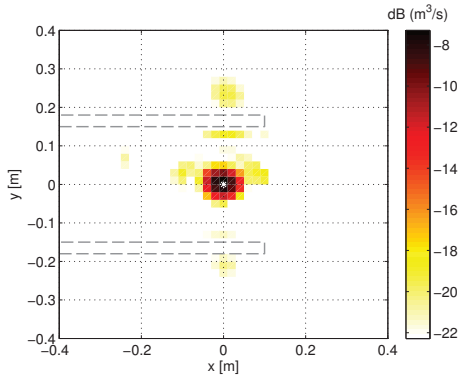


Figure 10: Volume velocity map integrated over the 4000-4500 Hz frequency band for a propagation computed by the image source method.

# 4 Experimental results

In this section, the propagation models described previously are used for the characterization of aeroacoustic sources. Above all, a limitation of the computed propagation matrix has been observed in practice. The propagation model accounting for the rigid surfaces tend to favor sources which are located at the proximity of the plates. The reason is that the radiation efficiency of equivalent sources close to the boundaries are considerably amplified due to the rigid surface. This is illustrated in Fig. 11, which shows the acoustic pressure that each source generates at a microphone position (indicated by a black dot in the figure). As a consequence, the acoustic imaging method identified the sources essentially at the proximity of plates. One approach to attenuate this effect is proposed here, which consists in applying a weighting to the system in Eq. (10). The weighting coefficients are proportional to the acoustic pressure that each source generates on the array and are computed as following [9]:

$$W_{ij} = \delta_{ij} \sqrt{\left\langle |\mathbf{g}_i|^2 \right\rangle}, \tag{12}$$

where $\delta_{ij}$ is the Kronecker delta, $\mathbf{g}_i$ is the $i$-th column of the propagation matrix $\mathbf{G}$ and $\langle \bullet \rangle$ means the average over the number of microphones. The aim of this weighting is to impose that each equivalent source generates a comparable pressure level on the array. In addition, an aperture function as discussed in ref. [7], is applied in order to attenuate the contribution of equivalent sources near the boundaries of the source plane.

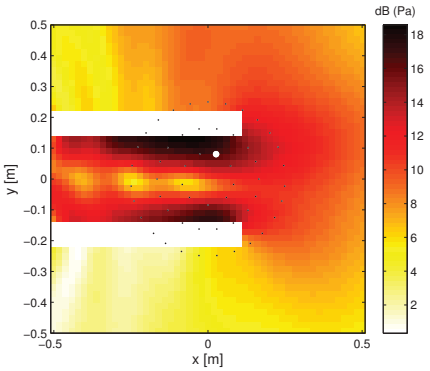


Figure 11: Acoustic pressure that each equivalent source generates at the position of a single microphone (indicated by a white dot). The frequency is 1500 Hz.

In a first experimental configuration, a 6mm diameter rod is placed about one chord downstream of a NACA 0012 airfoil trailing edge. They are both located at the potential core of the rectangular jet. The airfoil has a chord of 10cm, a span of 30cm and is placed at a 0° angle of attack. A turbulence grid is placed upstream of the nozzle and the airflow speed is adjusted to 30 m/s. The acoustic pressure averaged over all microphones on the array is shown in Fig. 12.

The identification method presented above is used to reconstruct the source field on a plane parallel to the microphone array. The acoustic intensity is reconstructed on the plane containing both the airfoil and the rod and two integration regions are defined: (a) around the airfoil leading edge and (b) along the rod span. The estimates of

the acoustic power corresponding to the airfoil leading edge and the rod are shown in Fig. 13. We firstly point out that care must be taken to interpret the results at low frequencies because the spatial resolution of the reconstructed field may not be enough to discriminate between closely spaced sources (airfoil trailing edge and the rod for instance). The results in Fig. 13 indicate that at lower frequencies the turbulence interaction noise from the airfoil leading edge dominates, except at frequencies around the Strouhal peak, in which vortex-shedding noise radiated at the rod vicinity prevails.

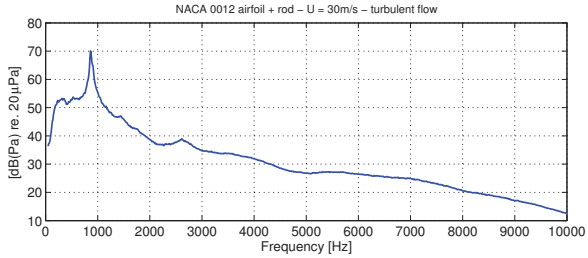


Figure 12: PSD of the averaged acoustic pressure over the microphone array.

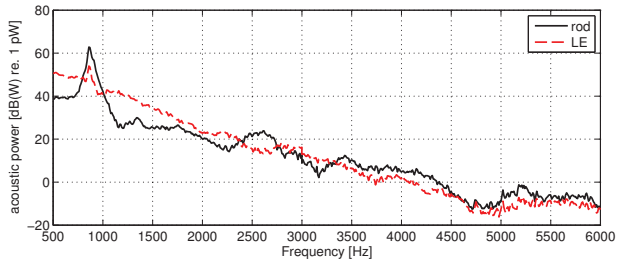


Figure 13: Estimate PSD of the acoustic power as integrated over the rod and the airfoil leading edge.

In order to illustrate the use of more realistic propagation models, we show in Figs. 14 and 15 the reconstructed source field considering a free-field propagation and computed by BEM. For the latter, we notice an increase of the spatial resolution and the identification of more discrete sources, as compared to the free-field case. Similar results were obtained for other frequencies.

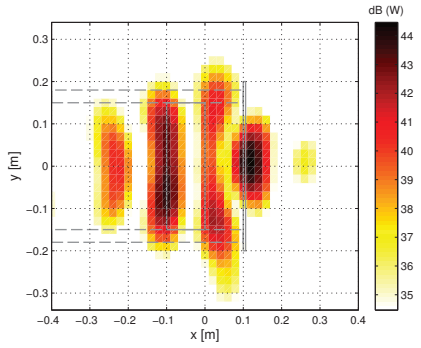


Figure 14: Acoustic intensity map integrated over the 2800-3000 Hz frequency band for a free-field Green's function. Flow direction is from left to right. The dynamic range is 10 dB.

In the second configuration, only the NACA 0012 airfoil at a 0° angle of attack is submitted to a laminar

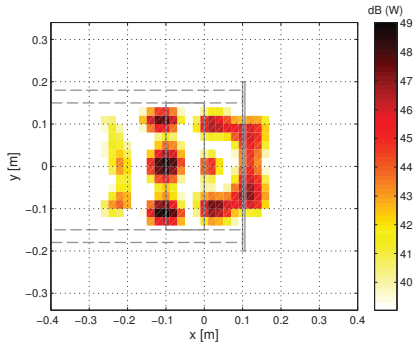


Figure 15: Acoustic intensity map integrated over the 2800-3000 Hz frequency band for a propagation matrix obtained by BEM. Flow direction is from left to right.

flow of speed 40 m/s. The PSD of the average pressure over the microphones is shown in Fig. 16. We can notice the emergence of a series of peaks related to the Tollmien-Schlichting instability waves developing on the airfoil. An acoustic feedback mechanism is responsible for the strong amplifications shown in Fig. 16 [10]. The identification method presented above is used to reconstruct the source field on the plane of the airfoil. The results for a frequency band around the prominent peak are obtained for a free-field Green's function (see Fig. 17) and for a propagation matrix computed by BEM (see Fig. 18). Contrary to the results for an artificial source, there is little difference between both cases. Similar results observed for other frequencies indicate that, in terms of localization, there is not significant difference between the free-field and more realistic propagation models in this particular case.

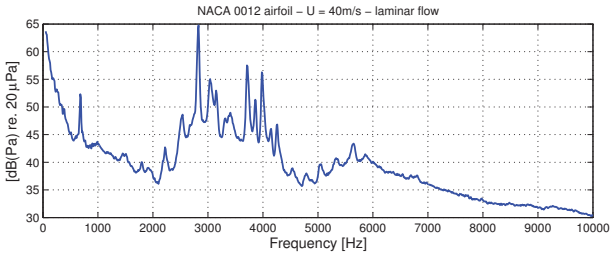


Figure 16: PSD of the averaged acoustic pressure over the microphone array.

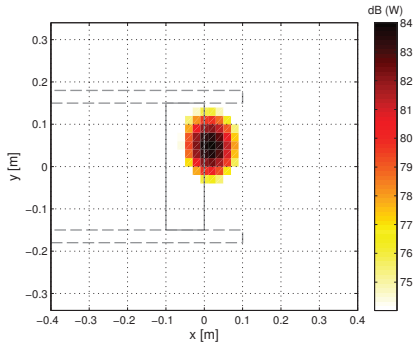


Figure 17: Acoustic intensity map integrated over the 2760-2900 Hz frequency band for a free-field Green's function. Flow direction is from left to right.

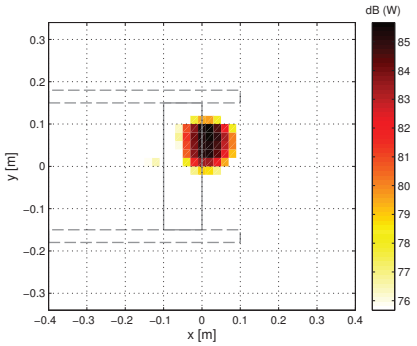


Figure 18: Acoustic intensity map integrated over the 2760-2900 Hz frequency band for a propagation matrix obtained by BEM. Flow direction is from left to right.

In order to analyze the results for a wide frequency band, the airfoil trailing edge is divided in three regions used for integrating the reconstructed acoustic intensity (see Fig. 19). The respective PSD corresponding to three regions is presented in Fig. 20. It can be observed that the region centered at midspan is usually responsible for the highest acoustic power and the regions at the proximity of the side-plates alternate in contribution as a function of the frequency.

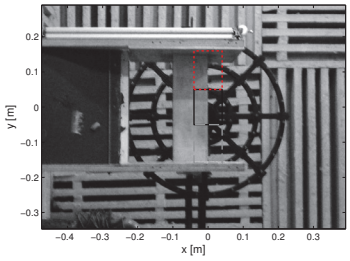


Figure 19: Different regions along the airfoil trailing edge used for the integration of the acoustic power.

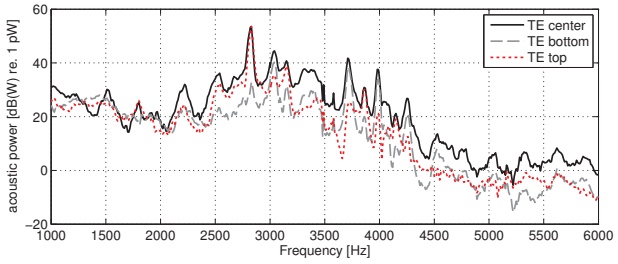


Figure 20: Estimate PSD of the acoustic power as integrated over different regions spanwise of the airfoil trailing edge.

# 5 Conclusion

In this work we have dealt with the application of acoustic imaging to the characterization of aeroacoustic sources measured in an anechoic open-jet wind tunnel. We have evaluated, in particular, the influence of the installation effects on the results of source identification. Validation measurements with an artificial source have shown a significant effect on the reconstructed field, which was attenuated by taking into account the geometry of the installation in the propagation model. In the case of aeroacoustic sources, although we notice an improvement on the spatial resolution, the differences between free-field and more realistic propagation models was not considerable. Further work could address the validity of neglecting the airfoil geometry and the nozzle lips on the numerical model.

# Remerciements

This work has been carried out within the framework of the project SEMAFOR supported by the FRAE (Fondation de Recherche pour l'Aéronautique et l'Espace). This work was also conducted in the framework of the LabEx CeLyA ("Centre Lyonnais d'Acoustique", ANR-10-LABX-60).

# References

[1] N. Chu, A. Mohammad-Djafari, and J. Picheral, "Robust bayesian super-resolution approach via sparsity enforcing a priori for near-field aeroacoustic source imaging," *Journal of Sound and Vibration*, vol. 332, no. 18, pp. 4369 – 4389, 2013.

[2] T. Suzuki, "L1 generalized inverse beam-forming algorithm resolving coherent/incoherent, distributed and multipole sources," *Journal of Sound and Vibration*, vol. 330, no. 24, pp. 5835 – 5851, 2011.

[3] B. A. Fenech, *Accurate aeroacoustic measurements in closed-section hard-walled wind tunnels*. PhD thesis, University of Southampton, June 2009.

[4] S. Moreau, C. Schram, and M. Roger, "Diffraction effects on the trailing edge noise measured in an open-jet anechoic wind tunnel," in *Thirteenth AIAA/CEAS Aeroacoustics Conference, Rome, Italy*, 2007.

[5] M. Roger and S. Moreau, "Diffraction and refraction effects in trailing-edge noise free-jet experiments," in *CFA/DAGA 2004 Congress, Strasbourg*, 2004.

[6] Q. Leclère, "Acoustic imaging using under-determined inverse approaches: Frequency limitations and optimal regularization," *Journal of Sound and Vibration*, vol. 321, no. 3-5, pp. 605 – 619, 2009.

[7] J. Antoni, "A bayesian approach to sound source reconstruction: Optimal basis, regularization, and focusing," *The Journal of the Acoustical Society of America*, vol. 131, no. 4, pp. 2873–2890, 2012.

[8] A. Pereira, *Acoustic imaging in closed spaces*. PhD thesis, INSA de Lyon, 2013.

[9] Q. Leclère, C. Pézerat, B. Laulagnet, and L. Polac, "Application of indirect measurement techniques to an operating diesel engine," in *Proceedings of ISMA 2004, Leuven, Belgium*, 2004.

[10] H. Arbey and J. Bataille, "Noise generated by airfoil profiles placed in a uniform laminar flow," *Journal of Fluid Mechanics*, vol. 134, pp. 33–47, 1983.